Journal of Catalysis 278 (2011) 253–265

Contents lists available at ScienceDirect

Journal of Catalysis

journal homepage: www.elsevier.com/locate/jcat

Thiotolerant $Ir/SiO_2–Al_2O_3$ bifunctional catalysts: Effect of metal–acid site balance on tetralin hydroconversion

Salim Nassreddine, Laurence Massin, Mimoun Aouine, Christophe Geantet, Laurent Piccolo *

Institut de recherches sur la catalyse et l'environnement de Lyon, IRCELYON, UMR 5256 CNRS & Université Lyon 1, 2 Avenue Albert Einstein, F-69626 Villeurbanne, France

ARTICLE INFO

Article history:
Received 28 July 2010
Revised 15 October 2010
Accepted 16 December 2010
Available online 26 January 2011

Keywords:
Iridium
Amorphous silica–alumina
Bifunctional catalysts
Ring opening
Tetralin
Thiotolerance
Comprehensive two-dimensional gas chromatography

ABSTRACT

The hydroconversion of tetralin over iridium nanoparticles supported on amorphous silica–alumina (ASA) has been investigated in a continuous high-pressure gas-phase micro-reactor in the presence of H_2S. In order to tune the Ir particle size, the bifunctional Ir/ASA catalysts have been submitted to sintering treatments. The samples have been characterized by HRTEM and XPS. From careful analysis of tetralin conversion products by comprehensive two-dimensional gas chromatography (GC×GC–MS) and NMR, compound families have been unambiguously distinguished. Hydrogenation, dehydrogenation, (saturated and aromatic) ring-contraction products, and (saturated and aromatic) one-ring-opening products are formed, without significant cracking. The catalysts exhibit stable activity in the presence of sulfur. As the mean particle size increases from 1.5 to 8 nm, the ring-opening/contraction selectivity increases dramatically. This effect is related to an increase of the acid/metal site ratio.

1. Introduction

The reduction in pollution and energy consumption by vehicles requires new technologies for the production of high-quality fuels. In the case of diesel regulations, cetane number (CN), which measures the fuel combustion efficiency, will have to increase in the next years (CN must be at least 51 since 2000 in Europe). Aromatics in diesel fuels produce particulates in the exhaust gases and, in addition, have poor ignition properties. Thus, their amount has to be reduced. The unprecedented demand of high-quality diesel, especially in Europe, gave birth to commercial upgrading technologies such as aromatics saturation (ASAT) [1] combined with, or following, deep hydrodesulfurization. However, the improvement of CN by ASAT is limited by the feedstock composition and cannot reach high values, since the formed naphthenic compounds present a modest increase in CN relative to their parent aromatic precursors. CNs of petroleum cuts increase with their paraffinic character as well as with their molecular weight. Thus, an additional route, complementary to ASAT, has been proposed, the so-called selective ring opening (SRO) route (see Fig. 1) [2,3].

Since compounds containing two fused six-membered rings constitute most of the aromatic/naphthenic feed, tetralin, naphthalene, and decalins (*cis* and *trans*) are often considered as model molecules representative of diesel fuels in SRO studies. In theory, the SRO reaction may lead to very high CNs but in practice, it is often limited to the opening of one ring, which in some cases may cause a dismal loss of CN [4]. The chemistry of SRO refers to several combined catalytic routes and requires in fact balanced metallic and acidic functions to achieve optimal performances, *i.e.*, reduce the number of rings while retaining the number of carbon atoms of the reactant molecule [5].

Concerning metal-catalyzed hydrogenolysis, an abundant literature demonstrates that three- to five-membered ring opening can be accomplished on group VIII metals and alloys [6–8]. The ring-opening ability depends on a number of factors, such as particle size, nature of the support, and nature of the cyclic compound (ring opening is much more difficult for six-membered rings than for five-membered rings). However, McVicker et al. have evidenced the unique properties of Ir for SRO, showing the propensity of this metal to cleave the C—C bond *via* the dicarbene mechanism [3]. Compared to single rings, opening of multiple-ring molecules has been far less studied due to the lower rate of this type of reactions and its increased complexity [5], but Ir has also been found efficient for hydrogenolysis of bicyclic naphthenes [3].

Carbocation cleavage on acidic catalysts is another way of achieving ring opening, mostly by β-scission. However, together with hydrogen transfer, transalkylation or disproportionation, it may produce more than 200 compounds and fast catalyst deactivation [9]. It has been shown that addition of a noble metal like Pt to

* Corresponding author. Fax: +33 472445399.
E-mail address: laurent.piccolo@ircelyon.univ-lyon1.fr (L. Piccolo).

0021-9517/$ - see front matter © 2010 Elsevier Inc. All rights reserved.
doi:10.1016/j.jcat.2010.12.008

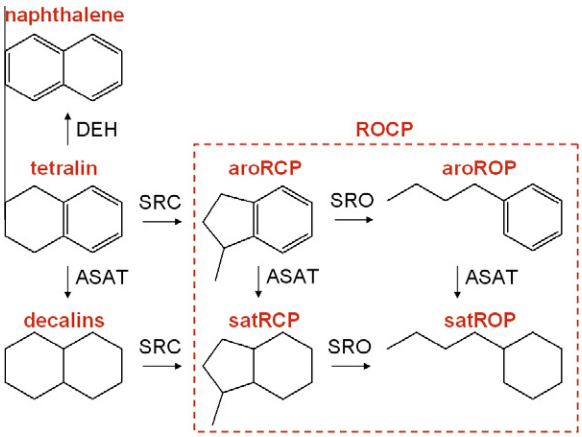

Fig. 1. Simplified reaction scheme showing the various product families for tetralin hydroconversion on Ir/ASA (only one representative product is displayed per family). DEH, ASAT, SRC, and SRO denote dehydrogenation, aromatics saturation, selective ring contraction, and selective ring opening, respectively. This scheme is not mechanistic (*e.g.*, SRO may occur without intermediate SRC).

acidic materials reduces the strength of Brönsted acid sites and significantly enhances isomerization and ring opening of decalin [10]. Unfortunately, the use of zeolites [9–16] can lead to undesirable non-selective cracking, side reactions and pore restriction issues. Thus, recent research has also focused on noble-metal catalysts supported on mesoporous silica-based materials [17–23]. In such bifunctional catalysts, although mild, the acidic function enables ring contraction, which can facilitate further hydrogenolysis of the C—C bond on metallic sites.

An additional important parameter is thiotolerance, *i.e.*, catalyst resistance to the presence of sulfur in the feed. In dual-stage processes, noble metals can be used since H_2S pressure has been drastically decreased between the two reactors. Thus, the design of an optimal catalyst should consider the sulfur resistance toward residual H_2S (from 10 to 250 ppm, depending on the running parameters of the two-stage process and the performances achieved in the first hydrodesulfurization reactor). Interaction between metals and acidic supports favors thiotolerance, the electron transfer from the metal to the support weakening the metal—sulfur bond [5]. Unfortunately, most studies on model molecules do not consider the poisoning effect of H_2S, which notably affects the hydrogenation reaction [24] and possibly the hydrogenolysis reaction.

In order to take advantage of the unique selective hydrogenolysis properties of Ir combined with the ring-contraction ability of acidic catalysts and their benefic effect on metal thiotolerance, several works on SRO have used Ir-based catalysts containing modified supports [20,25,26] or promoters [22,27,28]. Again, multi-ring compounds have been studied to smaller extent, and only Infantes-Molina et al. have considered the tetralin/Ir system for SRO, using Zr–MSU as a support [20].

In the course of an extensive SRO study of Ir supported on amorphous silica–alumina, we have previously investigated in details the preparation of Ir/ASA catalysts [29] and the effect of support acidity (by tuning the Si:Al ratio in ASA) on tetralin hydroconversion properties [30]. In this article, we report on the structural properties of Ir/ASA and, using an advanced chromatographic technique, on the effect of Ir particle size on the catalyst performances.

2. Experimental

2.1. Materials preparation

Amorphous silica–alumina (ASA, commercial name SIRAL-40) was supplied by Sasol (formerly Condea). The as-received powder in hydrated form was activated by heating at 550 °C in air for 3 h. It resulted in dehydration of the powder and transformation of the AlO(OH) (boehmite) alumina part to γ-Al_2O_3. The silica part is in the form of amorphous islands dispersed on alumina. The average particle size, BET surface area, pore volume, and pore diameter are 50 μm, 500 $m^2\ g^{-1}$, 0.90 mL g^{-1}, and 6.4 nm, respectively. The silica concentration measured by inductively coupled plasma optical emission spectrometry (ICP-OES, Activa – Horiba Jobin Yvon) after dehydration was 36 wt.% silica (*i.e.*, Si:Al atomic ratio 0.48). Characterizations of the SIRAL product range can be found elsewhere [30,36].

The catalysts were prepared by incipient wetness impregnation of ASA with iridium trisacetylacetonate ($Ir(C_5H_7O_2)_3$, Sigma–Aldrich, purity 97%) dissolved in toluene using the concentration needed to obtain an Ir loading of 1.0 wt.%. After impregnation, the samples were dried at 120 °C overnight and in some cases calcined at 350 °C in air flow (60 mL min^{-1}) for 3 h (heating rate from room temperature: 2 °C min^{-1}). In all cases, they were reduced in H_2 flow (60 mL min^{-1}) at a temperature comprised between 350 and 550 °C for 6 h. The sample characteristics are reported in Table 1.

Once the preparation was optimized [29], leading to well-dispersed nanoparticles (mean diameter 1.5 ± 0.2 nm), a sintering procedure was applied to obtain larger particles. To this aim, the sample was heated to 500–700 °C for 4–6 h in 2 vol.% H_2O balanced in N_2 (by flowing 60 mL min^{-1} of N_2 at atmospheric pressure through a saturator containing liquid water at RT), similar to the treatment applied by Balcon et al. [31]. Samples sintered at 500 °C and 700 °C are denoted S500 and S700, respectively (Table 1).

2.2. Materials characterization

2.2.1. Transmission electron microscopy

The size distribution of Ir nanoparticles was determined by high-resolution transmission electron microscopy (HRTEM, Jeol JEM-2010 and JEM-2010F).

Carbon replicas were prepared by the following method. A dispersion of the catalyst crushed in ethanol was deposited over a cleaved mica plate, which was then covered with a carbon film

Table 1
Characteristics of the catalysts.

Catalyst pretreatment[a]	Ir loading[b] (wt.%)	Ir particle size[c] (nm) surface-weighted size (nm) volume-weighted size (nm)
C350R350	0.80	d = 7.8 ± 4.3; 1.4 ± 0.2 d_{surf} = 11.0 ± 3.5 d_{vol} = 12.1 ± 3.5
R350	0.96	d = 1.4 ± 0.2 d_{surf} = 1.5 ± 0.2 d_{vol} = 1.5 ± 0.2
R350 + C350 + R350	0.96	Idem
R450	0.90	d = 1.5 ± 0.4 d_{surf} = 1.7 ± 0.4 d_{vol} = 1.8 ± 0.3
R550	0.90	d = 1.4 ± 0.3 d_{surf} = 1.5 ± 0.2 d_{vol} = 1.6 ± 0.3
R350 + S500 + R350 (=S500)	0.81	d = 4.9 ± 1.2; 1.4 ± 0.3 d_{surf} = 5.4 ± 1.2 d_{vol} = 5.7 ± 1.2
R350 + S700 + R 350 (=S700)	0.90	d = 6.7 ± 1.9; 1.3 ± 0.2 d_{surf} = 7.8 ± 2.0 d_{vol} = 8.4 ± 2.2

[a] Cx denotes calcination in air flow for 3 h at *x* °C, Ry means subsequent reduction in H_2 flow for 6 h at *y* °C, Sz means sintering at *z* °C in 2 vol.% H_2O in N_2.
[b] Determined by ICP-OES.
[c] Mean particle size and standard deviation determined from TEM images (see Section 2.2.1 for details).

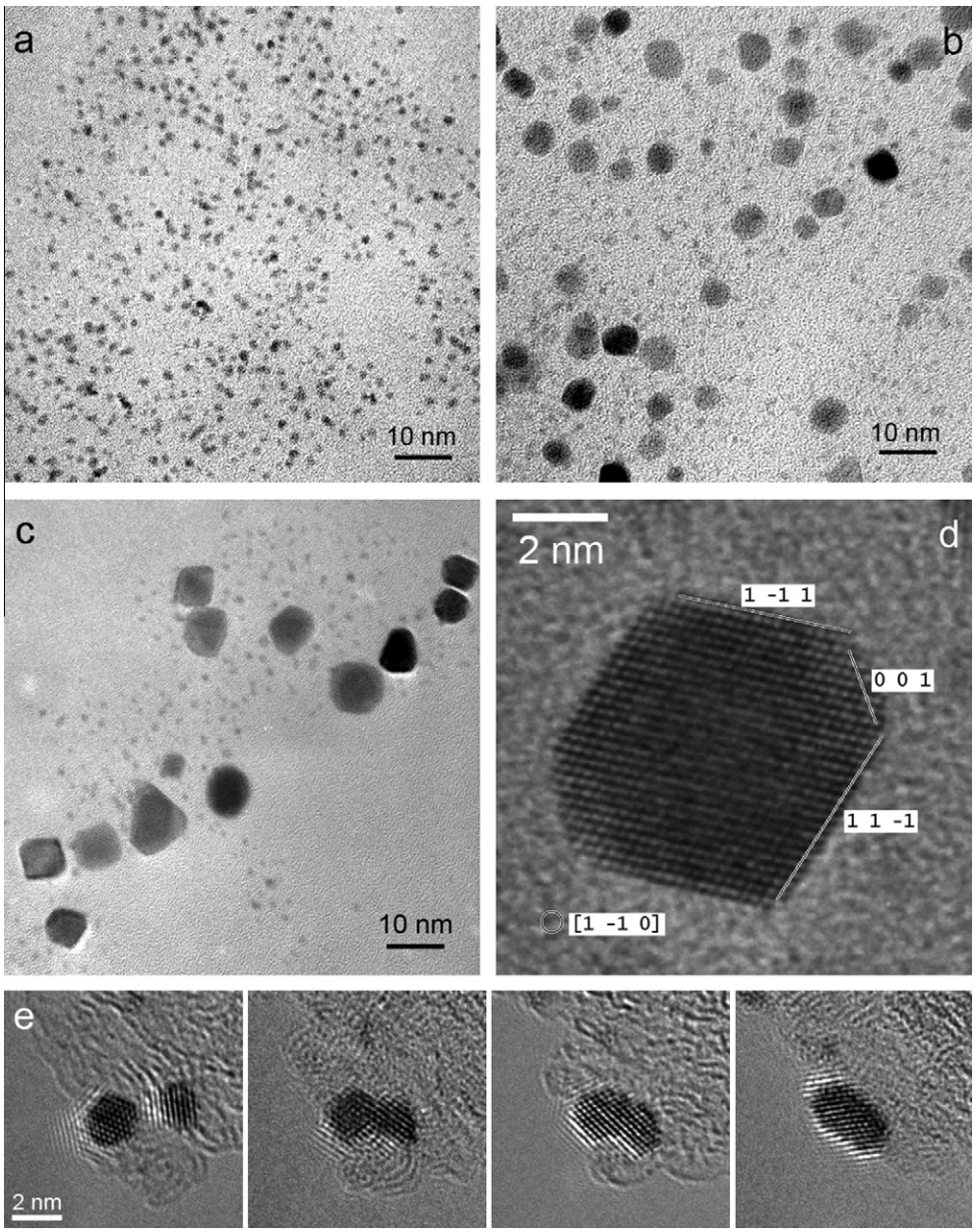

Fig. 2. Transmission electron micrographs of Ir nanoparticles prepared by impregnation of ASA with $Ir(acac)_3$ followed by: (a) reduction at 350 °C (R350 sample); (b) sintering of R350 at 500 °C and reduction at 350 °C (S500 sample); (c) sintering of R350 at 700 °C and reduction at 350 °C (S700 sample); (d) HRTEM image of S500; (e) series of HRTEM images recorded every 1 min for S500. The images in (a–d) and (e) have been acquired with Jeol JEM-2010 and Jeol JEM-2010F, respectively.

and kept in a solution containing water, acetone and fluorhydric acid for 24 h. After having dissolved the support, the carbon film containing the particles was deposited on standard holey carbon-covered copper TEM grids. Size histograms were calculated from the statistical treatment of the TEM micrographs, by analyzing 300–700 particles.

Depending on the topic of interest (catalysis, XPS, XRD, etc.), it may be relevant to average the particle sizes over the surface distribution $n_i d_i^2$ ("surface-weighted mean size" $\langle d\rangle_{surf} = \Sigma n_i d_i^3 / \Sigma n_i d_i^2$, where n_i is the number of particles in the diameter range d_i) or the volume distribution $n_i d_i^3$ ("volume-weighted mean size" $\langle d\rangle_{vol} = \Sigma n_i d_i^4 / \Sigma n_i d_i^3$), instead of solely averaging the numeric distribution n_i (classical mean size $\langle d\rangle = \Sigma n_i d_i / \Sigma n_i$). The differences between the three averaging methods are important in the case of asymmetric or bimodal size distributions. In Table 1, the values of $\langle d\rangle$, $\langle d\rangle_{surf}$, and $\langle d\rangle_{vol}$ and the corresponding standard deviations have been refined by Gaussian fittings of the size distributions. Fig. 3 only reports surface-weighted size histograms, which are relevant to catalysis.

2.2.2. X-ray photoelectron spectroscopy

XPS was performed in a Kratos Axis Ultra DLD spectrometer, equipped with a hemispherical analyzer and a state-of-the-art delay line detector. A monochromated Al Kα X-ray source (1486.6 eV, 150 W) with charge neutralization was used. An *in situ* cell coupled to the ultra-high vacuum analysis chamber allowed us to heat the samples under H_2 or air flow for 2 h at atmospheric pressure before XPS analysis. Spectra were measured at the normal to the sample surface (probed surface 0.2 mm^2). To remove the contribution of charging effects, high-resolution spectra were referenced to the Al 2p peak at 74.5 eV. Binding energies were determined with an accuracy of ±0.2 eV. Shirley background subtraction and 70%

Gaussian × 30% Lorentzian fitting were used to analyze the spectra.

2.3. Catalytic testing

Experiments were carried out in a continuous gas-phase flow fixed bed catalytic micro-reactor based on the system described in Ref. [32]. The reactor itself is constituted by a Pyrex tube (10 mm internal diameter), containing a porous disk supporting the catalyst bed and located in a U-shaped stainless steel tube. Note that Pyrex prevents sulfur storage by the steel tube [33]. The reactor temperature was measured with a thermocouple located in the catalyst bed. Tetralin (1,2,3,4-tetrahydronaphthalene) was purchased from Sigma–Aldrich (>99% purity). Non-diluted tetralin was introduced in the reactor by vapor saturation of a hydrogen stream using a high-pressure saturator. The hydrocarbon partial pressure (12 kPa before dilution in H_2) was fixed by a temperature-controlled condenser (133 °C for tetralin). The H_2S molar concentration was varied between 0 and 200 ppm by diluting a mixture (Praxair) of 500 ppm H_2S and H_2 into the main H_2 flow (Air Liquide, 5 N purity). A back-pressure regulator placed at the outlet of the reactor enabled an accurate control of the total pressure (4 MPa). The temperature of the reactor inlet/reactor outlet/back-pressure regulator system was set at 180 °C in order to avoid hydrocarbon condensation in the gas lines. The standard reaction conditions consisted of a hydrogen pressure of 4 MPa, a partial pressure of tetralin of 6 kPa (*i.e.*, 45 Torr, H_2/hydrocarbon molar ratio = 670) and a temperature range of 250–350 °C. 10–50 mg of catalyst and a flow rate of 20–200 mL min^{-1} were used in the tests (contact time range 2–100 s, standard contact time 20 s). Prior to each activity measurement, the samples were reduced *in situ* in hydrogen flow (90 mL min^{-1}) at 350 °C for 2 h (heating rate from room temperature: 2 °C min^{-1}).

The gas composition at the reactor outlet was determined by on-line gas sampling and gas chromatography (GC). The GC was a HP 5890 II equipped with a flame ionization detector (FID) and a HP-1 column (25 m × 0.2 mm × 0.5 μm). A stabilization time of 9–15 h was used prior to activity measurements.

Tetralin conversion rates (r_{THN}, mol s^{-1} g^{-1}) were calculated using pseudo-first order kinetics and a plug flow reactor model, according to the following formula:

$$r_{THN} = -\frac{F_{THN}}{m_{cat}} \ln(1 - \chi_{THN}) \quad (1)$$

where F_{THN}, χ_{THN}, and m_{cat} stand for tetralin molar flow rate, tetralin conversion and catalyst mass, respectively. In conventional GC, hydrocarbon conversion was calculated from $(A_{total} - A_{HC})/A_{total}$, where A_{total} is the total GC peak area (corresponding to all the products + unconverted hydrocarbon) and A_{HC} the peak area for (unconverted) hydrocarbon. The yield to product i (Y_i) is defined as A_i/A_{total}, where A_i is the peak area for product i. The selectivity to product i is calculated from Y_i/χ_{HC}. GC response is similar for all C_{10} products; hence, the yields or selectivities given in mol.% or wt.% are similar for these products.

2.4. Products analysis

2.4.1. Comprehensive two-dimensional gas chromatography

The GC×GC system [34] was installed in a modified 6890 N gas chromatograph (Agilent) equipped with a two-stage thermal modulator (Zoex Corporation). A single low-temperature valve mounted outside the GC oven controls the cold jet, which provides narrow chemical pulses. The modulator accumulates samples eluting from the first column for a period equal to 1/3 to 1/4 of the duration of an individual peak. A modulation period of 12 s was used here. The secondary column effluent was analyzed using quadrupole mass selective detector 5975B (Agilent). The two columns were Phenomenex ZB1MS (length 30 m, internal diameter 0.25 mm, film thickness 1 μm) and Varian VF17MS (length 3 m, internal diameter 0.1 mm, film thickness 0.2 μm). The temperature program for the first oven was 60 °C for 1 min, increase to 150 °C at 0.6 °C min^{-1}. For the second oven, it was 60 °C for 4 min, increase to 180 °C at 0.8 °C min^{-1}. The sample (0.3 μL) was injected at

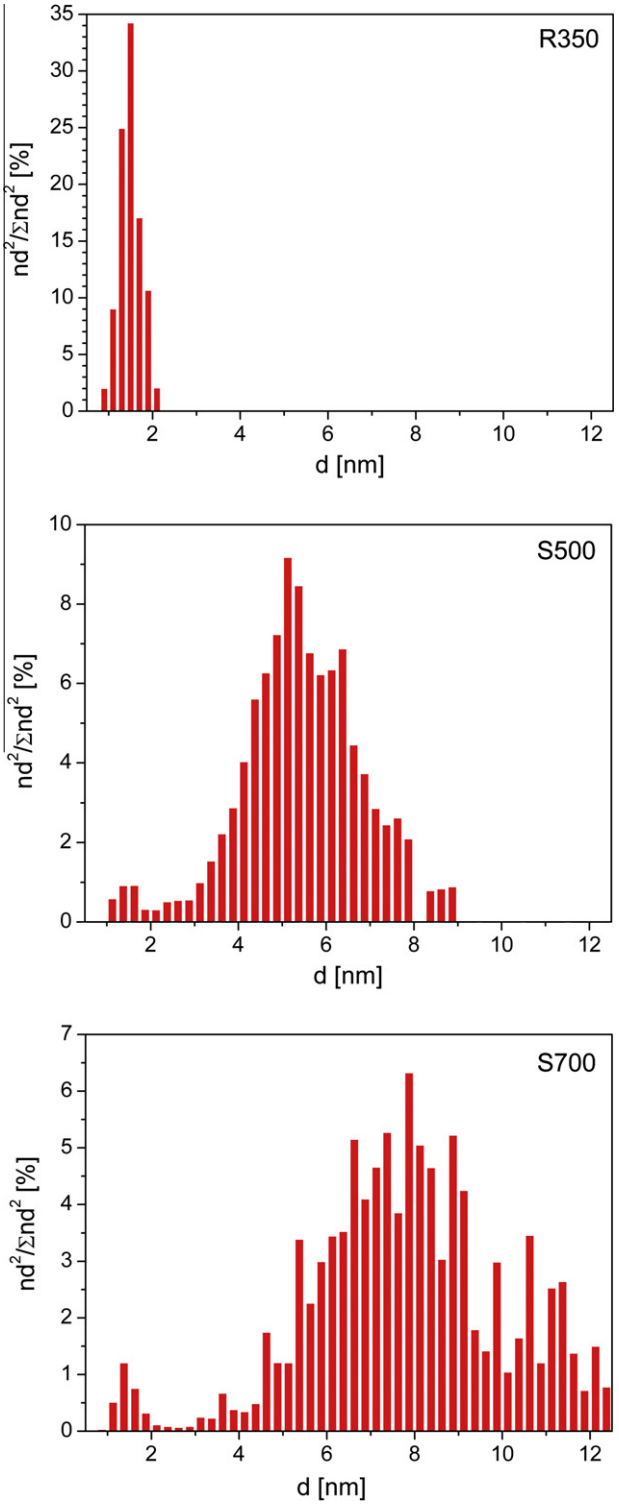

Fig. 3. Surface-weighted size distributions for R350 (318 particles analyzed), S500 (462 particles analyzed), and S700 (664 particles analyzed) samples.

280 °C with a split ratio of 250 at a constant He flow rate of 1.2 mL min^{-1}.

Molecules were separated on the basis of independent chemical properties (orthogonal separation conditions): volatility for the first column and polarity for the second one. The raw signal (total ionic current) of a GC×GC–MS experiment is a time-ordered series of second-dimension chromatograms. The data analysis software (GC Image, Zoex Corporation) constructs a three-dimensional chromatogram by placing these chromatograms side by side (the third axis represents the MS detector response) [35]. The concentration of a compound is proportional to the volume of the corresponding 3D peak (so-called "blob"). For first-sight product identification, the NIST Mass Spectral Search Program based on the NIST08 MS library and combined with GC Image was used.

Depending on the reaction conditions, between *ca.* 40 and 80 products of tetralin ($C_{10}H_{12}$) hydroconversion on Ir/ASA were detected by GC×GC–MS. The following compound families could be identified (Section 3.2.1):

- Dehydrogenation product: naphthalene ($C_{10}H_8$).
- Hydrogenation products: *trans*- and *cis*-decalins ($C_{10}H_{18}$).
- Cracking products are molecules with less than 10 carbon atoms. They are present only in some specific cases (selectivity always lower than 7%).
- Heavy products containing 11 carbon atoms (essentially methyl-tetralins and methyl-naphthalenes) are present in trace amounts (<0.5% selectivity). Thus, they have been neglected in the analysis of catalytic performances.
- Ring-opening/contraction products (ROCPs):
  Ring-contraction products (RCPs) are multi-ring compounds with at least one five-membered naphthenic ring. They can be subdivided in saturated ring-contraction products (satRCPs, $C_{10}H_{18}$ decalin skeletal isomers) and aromatic ring-contraction products (aroRCPs, $C_{10}H_{12}$ methyl-indans).
  Ring-opening products (ROPs) are one-ring compounds. They can be subdivided in saturated ring-opening products (satROPs, $C_{10}H_{20}$ alkyl-cycloalkanes) and aromatic ring-opening products (aroROPs, $C_{10}H_{14}$ alkyl-benzenes).

As discussed in Section 3.2.1, conventional GC (combined with the catalytic bench) is not able to discriminate all the products. Decalin skeletal isomers and ROPs appear coeluted in conventional chromatograms; thus, bidimensional GC is required for ROP separation. Such analysis was performed in a selected series of experiments. Otherwise, the products were grouped in five categories: naphthalene, *cis*-decalin, *trans*-decalin, ROCPs, and cracking products. Fig. 1 summarizes the above classifications and illustrates in a simplified way the links between the compounds families.

2.4.2. Nuclear magnetic resonance

^1H and ^{13}C NMR analyses were performed with a Bruker Avance 250 spectrometer on tetralin hydroconversion samples dissolved in $CDCl_3$ solvent, using tetramethylsilane as reference. ^1H NMR spectra were collected at 250.13 MHz, using 30° pulse (3 μs), 1 s relaxation delay, and 16 scans. ^{13}C NMR spectra were collected at 62.89 MHz using inverse-gated decoupling, 30° pulse, 2 s relaxation delay, and 2048 scans.

3. Results

3.1. Structural characterization of Ir/ASA catalysts

The ASA support containing 40 wt.% of silica (Sasol SIRAL-40) has been selected from a series of ASAs ranging from 5 to 70 wt.% of silica. Indeed, Ir/SIRAL-40 exhibits the highest Brönsted acidity (in agreement with a work on the SIRAL series [36]) as measured by infrared spectroscopy of adsorbed pyridine and shows the best performances in terms of activity and selectivity [30].

3.1.1. TEM study

The preparation/characterization data relative to the catalysts used in the present study are reported in Table 1. The target Ir loading of 1 wt.% was reached in all the cases, within 20%. After impregnation of ASA with $Ir(acac)_3$, two types of treatments were assessed. They consisted either of calcination in air flow at 350 °C followed by reduction in H_2 flow at 350 °C (sample denoted C350R350) or direct reduction at 350–550 °C (R350-R550). From the calcination–reduction treatments, small particles (mean size 1.5 nm) coexist with larger ones (~10 nm), as discussed in Ref. [29]. In contrast, the reduction-only pretreatment leads to a homogeneous size distribution centered at 1.5 nm, with a relative standard deviation smaller than 20% (Figs. 2a and 3a). The reduction temperature, between 350 and 550 °C, has no effect on Ir particle size (Table 1).

Having observed that the C350R350 sample was more selective to ring-opening products than the R350 sample, we tuned the Ir particle size by a sintering procedure (see Section 2.1). Heating the R350 samples in a wet atmosphere at 500 °C and 700 °C has led to the samples shown in Fig. 2b (S500 sample) and Fig. 2c (S700 sample), respectively. Although some particles remain non-sintered (mean size 1.4 nm), most of the particles are larger with mean sizes ($\langle d \rangle_{surf}$) of 5.4 nm and 7.8 nm for S500 and S700, respectively (see Table 1). As shown by the surface-weighted size distributions in Fig. 3, the contribution of small particles to the overall iridium surface of sintered samples is negligible.

In the S500 sample, the predominant shape is that of the particle shown in Fig. 2d. By comparing this image to the very similar one acquired by Gontard et al. with aberration-corrected TEM and wavefunction reconstruction (for platinum) [37], we conclude that our Ir nanoparticle is a thermally equilibrated truncated octahedron observed along the [1–10] direction. Sintering at 700 °C (S700) leads to well-faceted particles, but in some cases with "kinetic shapes", *i.e.*, for such sizes the temperature appears insufficient for particles to reach their equilibrium shape within the experiment duration (<6 h). Small particles (both in non-sintered and sintered cases) are truncated-octahedral, as illustrated by Fig. 2e for S500. In addition, this series of HRTEM images shows the electron beam-assisted coalescence of two particles. This phenomenon could be observed here by chance, since it was rarely occurring in the analyzed areas. The two particles sinter *via* contact of (1 0 0) planes. In the fourth image of Fig. 2e, the particle formed is single-crystalline.

3.1.2. XPS study

We have performed XPS analyses of calcined-reduced (C350R350, Fig. 4a), reduced (R350, Fig. 4b), reduced-calcined (R350-C350, Fig. 4c), and reduced-sintered (R350-S700, Fig. 4d) Ir/ASA samples. The 4f doublet was fitted with four components (two for $4f_{5/2}$ plus two for $4f_{7/2}$); the fit results for $4f_{7/2}$ are reported in Table 2. For bulk materials, $4f_{7/2}$ core level for metallic Ir appears at 60–61 eV, while that for oxidized Ir appears at higher energies [38–40]. The $4f_{7/2}$ component at 60.1–60.6 eV is thus ascribed to metallic Ir, while the contribution at 61.1–61.7 eV is assigned to Ir atoms in contact with the oxide support, giving rise to an oxidic state denoted $Ir^{\delta+}$. Our energy values for the Ir^0-$4f_{7/2}$ component (E_1) are close to what was found for Ir/SiO_2 catalysts (60.3–60.5 eV) [27,41].

As shown by Fig. 4b and Table 2, the core levels for R350 are 0.6 eV higher than those for C350R350 and the oxide contribution is larger (62% vs. 41%), both due to a proportionally larger influence of the support on Ir oxidation state in the case of R350, as expected

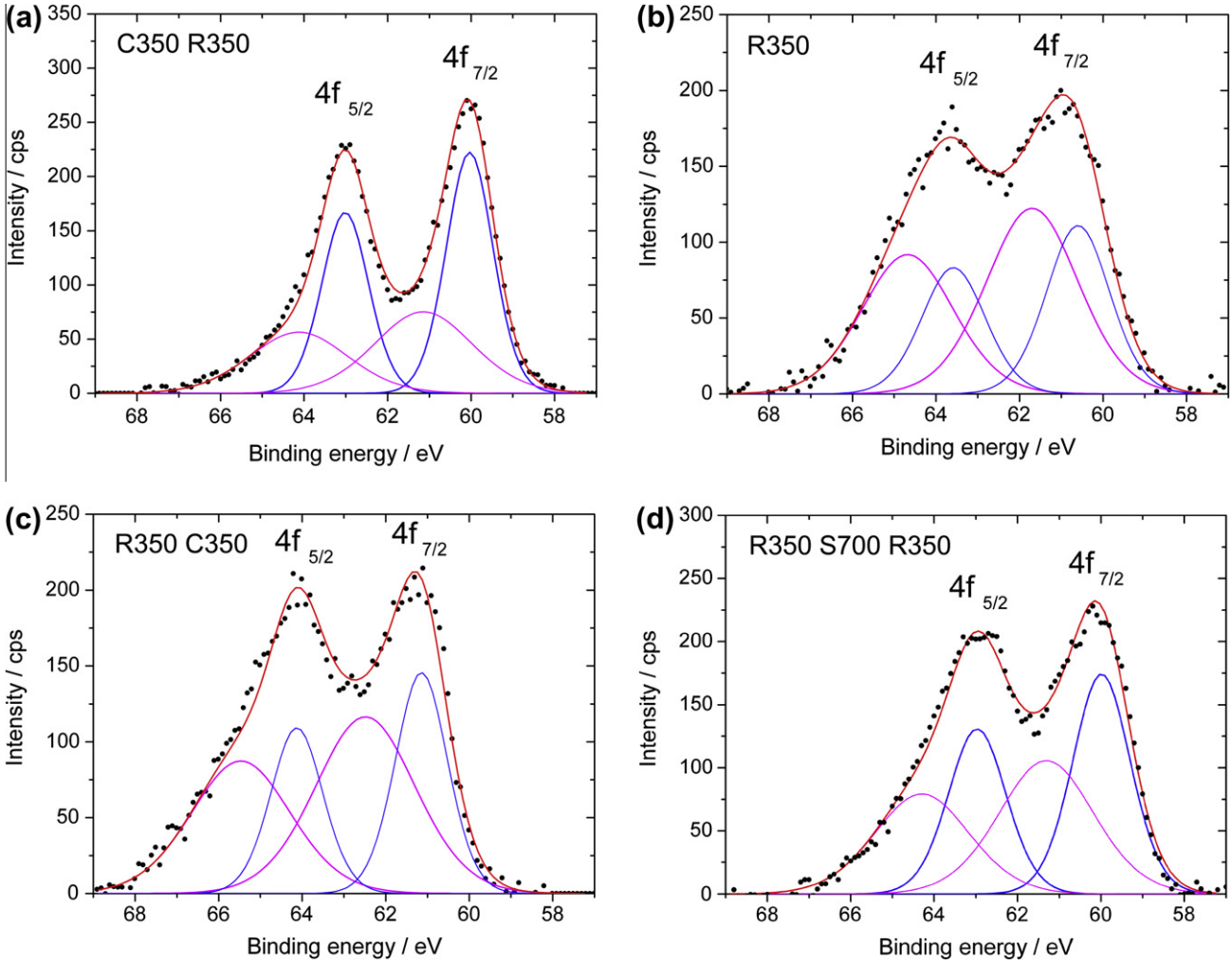

Fig. 4. X-ray photoelectron spectra (Ir 4f core levels) for: (a) C350R350 sample; (b) R350 sample; (c) R350 sample calcined in air; (d) S700 sample, further reduced *in situ* in H_2.

Table 2
Results of the XPS analysis ($4f_{7/2}$ core level).

Catalyst pretreatment	d_{surf} [a] (nm)	E_1 [b] (eV)	ΔE_1 [b] (eV)	E_2 [b] (eV)	ΔE_2 [b] (eV)	E_3 [b] (eV)	ΔE_3 [b] (eV)	$Ir^{\delta+}$ fraction [c] (%)
C350R350	11	60.0	1.4	61.1	2.9	–	–	41
C350R350 + R350 *in situ*	–	60.0	1.3	61.5	3.0	–	–	44
R350	1.5	60.6	1.9	61.7	2.7	–	–	62
R350 + C350	–	–	–	61.1	1.5	62.5	2.9	60
S700 + R350 *in situ*	7.8	60.0	1.7	61.3	2.8	–	–	50

[a] Surface-weighted Ir particle size, determined by TEM (from Table 1).
[b] E and ΔE denote peak energy and full width at half-maximum of the XPS fit peaks shown in Fig. 4, respectively.
[c] Partially oxidized Ir fraction given by the relative area of the peak at energy E_2.

for smaller nanoparticles.[1] Besides, the +0.6 eV energy shift and the +0.5 eV peak broadening are ascribed to a finite size effect, as observed for Pd nanoparticles supported on carbon [42].

Calcination in air of R350 gave rise to the disappearance of the metallic component at 60.6 eV and the appearance of a component at 62.5 eV, as seen in Fig. 4c and Table 2 (R350-C350). Now, $Ir^{\delta+}$ (partially oxidized state due to metal-oxide interface, $\delta < 4$) and Ir^{IV} (bulk IrO_2 oxide)[2] contributions coexist. The interfacial contribution for the oxidized sample (60%) is logically nearly equal to that for the reduced sample (62%).

Finally, the XP spectrum for the sintered sample (S700) is shown in Fig. 4d. The energetic parameters (Table 2) are very similar to those for C350R350, and the $Ir^{\delta+}$ fraction is 50%. This value, intermediate between that for R350 (62%, $\langle d \rangle_{surf}$ = 1.5 nm) and

[1] Additional *in situ* exposure of C350R350 to pure H_2 flow at 350 °C did not significantly affect energy positions (Table 2), showing that iridium was not oxidized in ambient air.

[2] IrO_2 is the only well known Ir oxide and exhibits the rutile crystal structure. Ir_2O_3 would exhibit the corundum structure and be meta-stable. IrO_3 has also been reported, but would be highly volatile [32].

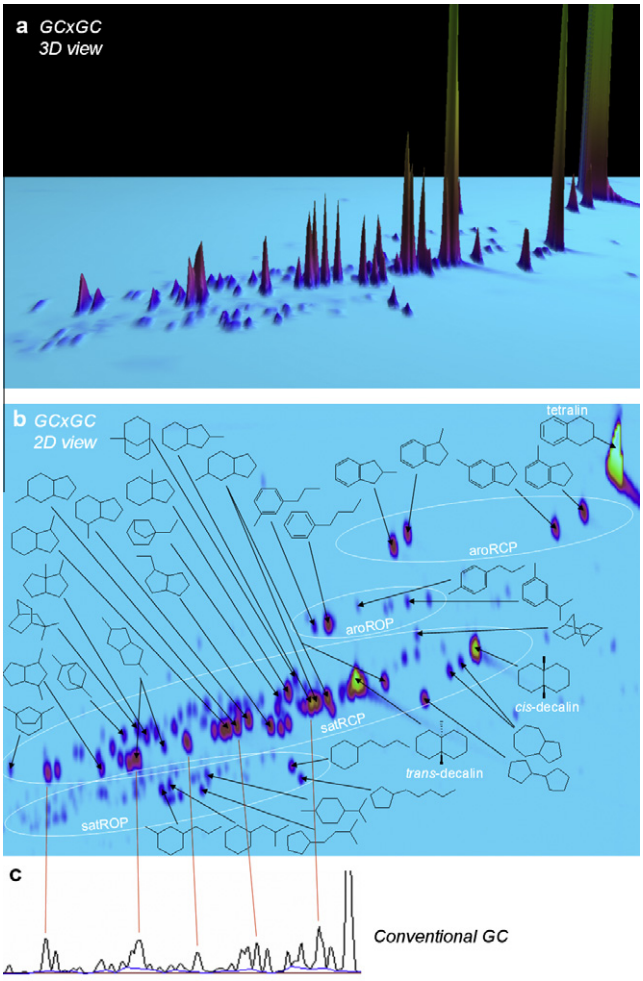

Fig. 5. (a) GC×GC–MS chromatogram (S700 sample, 50% tetralin conversion, 350 °C, 100 ppm H_2S) in 3D view. (b) Same chromatograph in 2D "top" view. Products families: aromatic ring-opening products (aroROP), saturated ring-opening products (satROP), aromatic ring-contraction products (aroRCP), saturated ring-contraction products (satRCP). MS-identified compounds are linked to the corresponding GC×GC blobs with arrows. The structure of stereoisomers is not detailed, except for decalins. (c) Conventional in-line GC chromatogram for the same experimental conditions.

C350R350 (41–44%, $\langle d \rangle_{surf}$ = 11 nm), is in-line with the intermediate particle size ($\langle d \rangle_{surf}$ = 7.8 nm).

3.2. Tetralin hydroconversion in the presence of sulfur

3.2.1. Nature of the reaction products

Fig. 5 shows an example of GC×GC–MS analysis. In such conditions that the ring-opening/contraction (ROC) selectivity is high, up to *ca.* 80 C_{10} compounds are detected. For numerous GC×GC blobs, the MS recognition databases proposed one-ring $C_{10}H_{18}$ compounds containing an endocyclic or exocyclic insaturation. However, ^{1}H NMR analyses of the samples rule out the presence of olefins, as shown by Fig. 6. As recently observed by Flego et al., MS databases commonly attribute cycloalkane fragmentation patterns to olefins [43]. This is due to the incompleteness of databases and the fact that the mass spectra of cyclic hydrocarbons become less and less characteristic with the increasing complexity of the molecule or in the presence of smaller than six-membered rings, which undergo ring opening to form initially 1-alkene ions [43]. In addition, few two-ring hydrocarbons are available as standards. By optimization of the GC separation conditions, careful analysis of

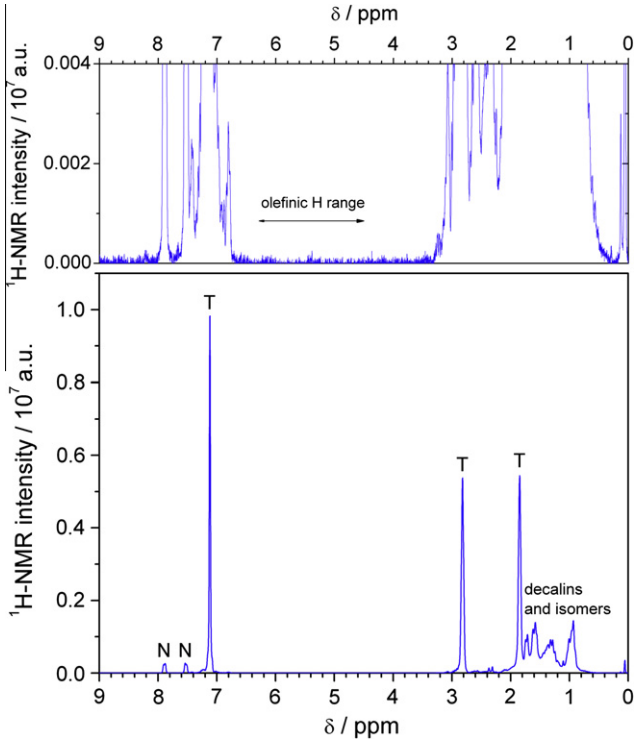

Fig. 6. ^{1}H NMR 250 MHz spectrum for products of tetralin hydroconversion on Ir/ASA (S700 sample, 70% tetralin conversion, 350 °C, 100 ppm H_2S). T and N stand for tetralin and naphthalene, respectively. The top graph shows a magnification by *ca.* 100 of the spectrum shown in the bottom graph.

the mass spectra and accurate comparison with literature data [44], we have been able to identify numerous products [45]. Fig. 5 shows that the products appear as separate families on the bidimensional chromatogram: satRCPs and decalins, aroRCPs, satROPs, and aroROPs (naphthalene is not visible in the figure). Let us present these four families (more details given in Ref. [45]):

- Saturated ring-contraction products (satRCPs): this is the most important family, containing polycyclic saturated compounds. The following satRCPs have been identified: two bicyclo[5.3.0]decanes, eight methyl-bicyclo[4.3.0]nonanes, 1-methyl-bicyclo[3.3.1]nonane, five dimethyl or ethyl-bicyclo[3.3.0]octanes, three dimethyl or ethyl-bicyclo[3.2.1]octanes, 2,2-dimethyl-bicyclo[2.2.2]octane and bicyclopentyl.
- Aromatic ring-contraction products (aroRCPs): this family contains the four methyl-indan position isomers.
- Saturated ring-opening products (satROPs): this family contains alkyl-cyclohexanes and alkyl-cyclopentanes. The most interesting ones in terms of diesel CN are *n*-butyl-cyclohexane (nBCH), the most abundant satROP, for which CN was evaluated to 49 [4] up to 62 [3], when compared to 10–20 for tetralin and 36–38 for decalin) and *n*-pentyl-cyclopentane (nPCP).
- Aromatic ring-opening products (aroROPs): this family contains alkyl-benzenes (*n*-butyl-benzene, so-called nBB, is the most abundant ROP).

These products are essentially the same as those obtained from tetralin conversion on more acidic catalysts like HY and Pt-HY [14]. The major exception lies in the absence of olefinic compounds in our case. In addition, with respect to Ref. [14], while bicyclo-heptanes and spiro[4.5]decane could not be formally identified here, *trans*- and *cis*-bicyclo[5.3.0]decanes were found only in our case. Besides, the nature of satRCPs is similar to that of decalin conversion products [9,10,43,45]. In fact, the main difference between our

Ir/ASA system and zeolitic ones is revealed by the greater number of products formed on zeolites, due to secondary isomerization (leading to highly branched C_{10} compounds), cracking/dealkylation (light $C_{<10}$ compounds), and transalkylation (heavy $C_{>10}$ compounds) [11–13].

The on-line products analysis has been performed with conventional GC, which does not allow the separation of all the products, as shown by the comparison of Fig. 5b with Fig. 5c, where only *ca.* 30 peaks are seen. In specific cases where additional GC×GC–MS analyses have not been carried out, it thus appears justified to group satRCPs, aroRCPs, satROPs, and aroROPs in a unique category, so-called ROCP in the present work, for the discussion of catalytic performances. The projection of the GC×GC pattern along the first dimension (*X*-axis in Fig. 5b) shows a close similarity (same blob sequence and similar intensities) with the corresponding conventional chromatogram in the ring-opening/contraction region (Fig. 5c), due to the use of the same type of non-polar capillary column in both instruments. This has allowed us to prevent any error when comparing GC on-line analyses with GC×GC–MS post-reaction analyses.

3.2.2. Effect of Ir particle size and reaction conditions on catalytic performances

The results of a complete catalytic test at 350 °C for the reference R350 sample are shown in Fig. 7. It illustrates the influence of time-on-stream on tetralin conversion and product yields for various H_2S concentrations. After the initial period (~8 h) during which the strongest acid sites are gradually deactivated, cracking becomes lower than 1%. Then, Ir/ASA exhibits a high stability, irrespective of H_2S concentration.

When H_2S is already present, tetralin conversion moderately decreases as H_2S concentration increases and the H_2S poisoning effect appears quasi reversible, since tetralin conversion is 89% (tetralin conversion rate 3.7 μmol g^{-1} s^{-1}) at 50 ppm H_2S, decreases to 67% (rate 1.9 μmol g^{-1} s^{-1}) at 200 ppm, and increases back to 85% (rate 3.3 μmol g^{-1} s^{-1}) when returning to 50 ppm.

Experiments at lower contact time, in which tetralin conversion in S-free conditions were below 100% (84–93%), have also been performed (same catalyst, temperature, and reactant pressures as here) [30]. They show that the tetralin conversion is divided by 2 upon addition of 50 ppm H_2S, whereas it is divided by 15 and 9

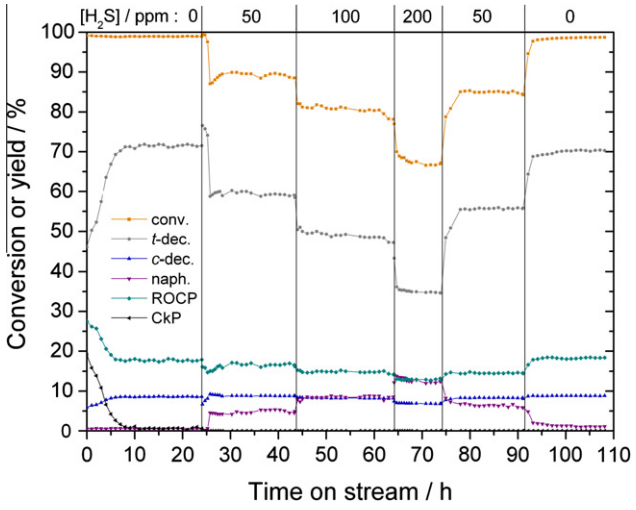

Fig. 7. Tetralin conversion and products yields vs. time-on-stream for tetralin hydroconversion at 350 °C over Ir/ASA (50 mg) under various H_2S concentrations. Conv., *t*-dec., *c*-dec., naph., ROCP, and CkP denote tetralin conversion, *trans*-decalin, *cis*-decalin, naphthalene, ring-opening/contraction products, and cracking products, respectively.

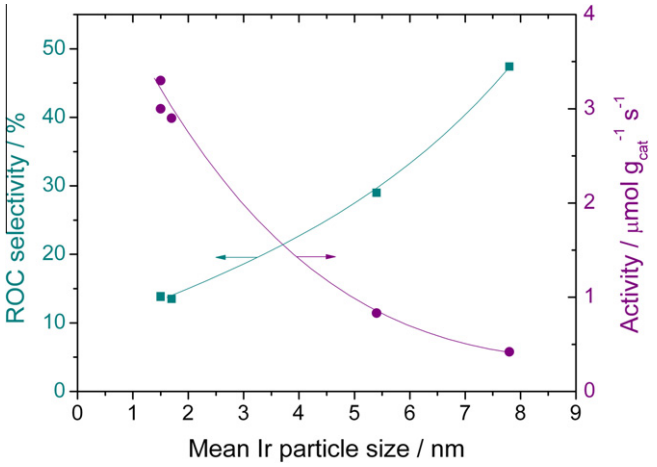

Fig. 8. Activity and selectivity to ring-opening/contraction products formed during tetralin hydroconversion (50% conversion, 350 °C, 100 ppm H_2S) vs. mean size ($\langle d \rangle_{surf}$) of ASA-supported Ir nanoparticles.

on Ir/SiO_2 and Ir/Al_2O_3, respectively. Moreover, Ir/ASA is the sole catalyst which recovers its activity after returning to S-free conditions [30], confirming that the acidic catalyst is by far the most sulfur-tolerant one.

Fig. 8 allows us to compare the various samples with respect to activity and ROC selectivity at isoconversion. As expected from TEM observations, no significant differences are observed between R350, R450 and R550 samples.[3] The selectivity to ROCPs is 14% for all three samples. The activity for tetralin conversion is 3 μmol g_{cat}^{-1} s^{-1}, which corresponds to a turnover frequency (TOF) of 0.09 molecule s^{-1} per surface Ir atom. By increasing the mean Ir particle size to 5.4 nm (S500) and 7.8 nm (S700), the ROC selectivity increases to 29% and 47%, respectively. Regarding the activity, the sintering of particles leads to a decrease of activity in an extent proportional to the loss of metallic surface. Indeed, the TOF remains essentially constant and equal to 0.08 ± 0.02 s^{-1}.

As shown by Fig. 9 (chromatograms) and Fig. 10 (analyzed GC data), two-dimensional gas chromatography enables a detailed comparison of products distributions between catalysts.[4] In Fig. 9, one can immediately observe that the number of products increases with Ir particle size. Three families of products can be distinguished: satRCPs (middle), aroROPs (top), and satROPs (bottom). The other compounds are not shown.

In Fig. 10, it can be seen that, at 50% of total conversion and in the presence of sulfur, the RC selectivity increases from 22% to 41%, and the RO selectivity increases from 0.8% to 5.1%, while the Ir particle mean size increases from 2.0 to 7.8 nm. The ratio of satRCPs among RCPs remains in the range 86–90% and that of satROPs in ROPs in the range 54–67%.

The increase of ROC selectivity with Ir particle size goes along with a decrease of selectivity to decalins (Fig. 10), with roughly constant *cis* isomer fraction equal to 24–27%. Besides, the cracking product fraction is 0 for the 2-nm-sized particles, 0.7% for the 5-nm-sized particles, and increases to 6.5% for the 8-nm-sized particles (not shown).[5] Hence, from a practical point of view, the S500 sample (5 nm) appears as a good compromise in terms of activity and ROC/cracking ratio.

[3] This proves that the reduction in H_2 at 350 °C is sufficient to completely remove acac ligands, as already reported [29].

[4] The so-called R350′ sample results from a partially unsuccessful attempt to sinter the R350 sample at 600 °C. For this 1.0 wt.% Ir/ASA catalyst, we obtain a particle size of d_{surf} = 2.0 ± 0.5 from TEM analysis.

[5] Light products were only analyzed by conventional GC.

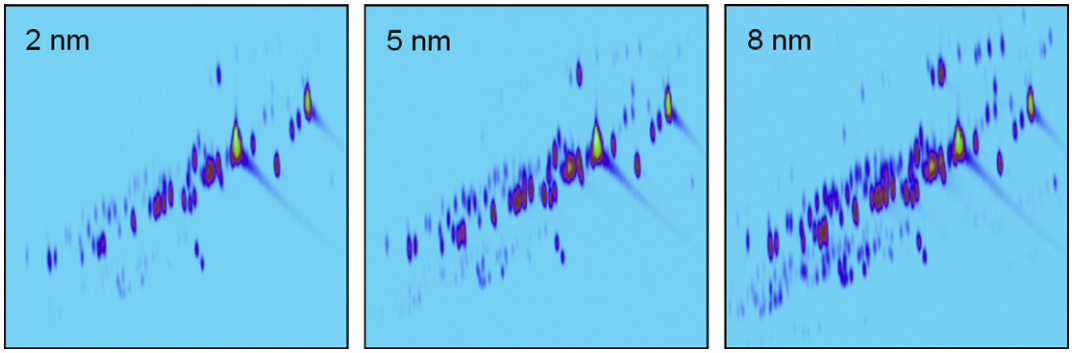

Fig. 9. GC×GC–MS analyses of samples issuing from tetralin hydroconversion (50% conversion, 350 °C, 100 ppm H_2S) on three different Ir/ASA catalysts (R350′, S500, and S700) characterized by their mean Ir particle size. Three product families appear on the chromatograms ("8 nm" chromatogram relates to the same sample as Fig. 5b).

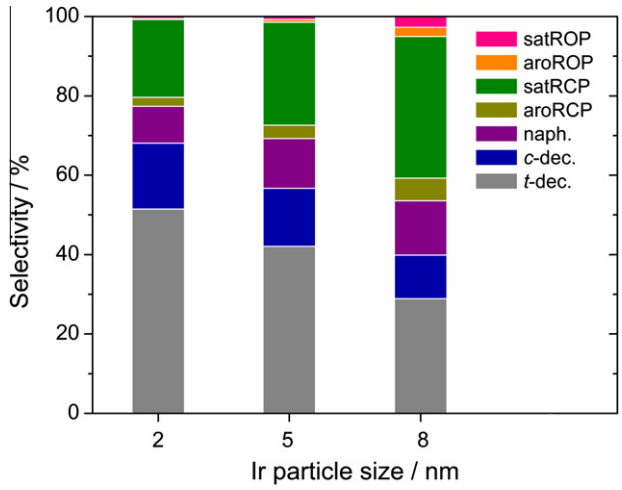

Fig. 10. Selectivity to tetralin hydroconversion C_{10} products, as determined from blob volumes in GC×GC patterns of Fig. 9.

A closer analysis of the ROP distribution shows that the major ROPs are those with an unsubstituted alkyl chain, which is favorable to CN [4]. Fig. 9 (with reference to Fig. 5) and Fig. 11 show that, whereas nBB, nBCH, and nPCP largely prevail in the case of small particles (65% of ROPs), many ROPs with shorter or branched chains appear when the largest particles are involved (the three above compounds represent 42% of ROPs in this case). Besides, while the fraction of nBCH and nPCP remains roughly constant and low (<0.3%), that of nBB increases from 0.2% to 1.7% as Ir particle size increases from 2.0 to 7.8 nm. This will be discussed in Section 4.2.

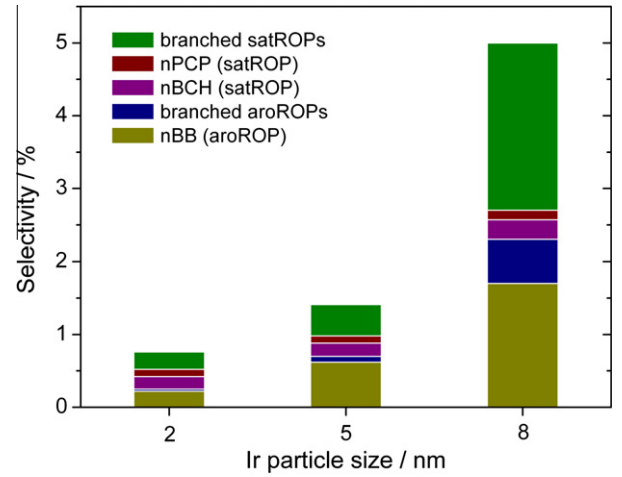

Fig. 11. ROP distribution, as determined from blob volumes in GC×GC patterns of Fig. 9. nBCH, nPCP, and nBB denote *n*-butyl-cyclohexane, *n*-pentyl-cyclopentane, and *n*-butyl-benzene, respectively. "Branched" products refer to those which do not have a single linear chain.

The effect of temperature on products distribution is reported in Fig. 12a and c. It appears that, for the reference sample (R350, $\langle d \rangle_{surf}$ = 1.5 nm), the ROC selectivity is zero below 300 °C, but increases with temperature above 300 °C (from 6% at 300 °C to 14% at 350 °C). The total hydrogenation selectivity is only slightly affected by temperature increase, whereas dehydrogenation decreases. Fitting the tetralin conversion rate (increasing from 0.7 μmol g^{-1} s^{-1} at 250 °C to 2.6 μmol g^{-1} s^{-1} at 350 °C) with an Arrhenius function (not shown) yields an apparent activation energy of 36 ± 4 kJ mol^{-1}. These results agree with those of Jiménez-Lopez and coworkers, who have found low ring opening rate below ~300 °C, and a maximum around 350 °C on mesoporous Rh-based catalysts [18,19]. However, in the case of the sample sintered at 700 °C (S700, $\langle d \rangle_{surf}$ = 7.8 nm), Fig. 12c shows that the ROC selectivity is 15% already at 250 °C and increases up to 47% at 350 °C. Thus, in the case of sintered samples, it is possible to decrease the working temperature and so reach relevant industrial conditions.

Fig. 12b and d show that, irrespective of the Ir particle size, the increase of H_2S concentration has no effect on ROC selectivities. Finally, Fig. 13 summarizes the results concerning Ir/ASA steady-state activity in the presence of increasing concentrations of H_2S. Fitting tetralin conversion rate vs. H_2S concentration with power functions ($r_{tetralin} \propto C_{H_2S}^{x}$) has allowed us to estimate pseudo-orders (x) for the evaluation of catalyst thiotolerance. x appears insensitive to Ir particle size. This will be commented in Section 4.2.

4. Discussion

4.1. Catalytic performances

Iridium combined with amorphous silica–alumina efficiently catalyzes tetralin ring saturation, contraction, and opening in the presence of H_2S. The selectivity toward ring-opening/contraction products increases with Ir particle size. At 350 °C, under large hydrogen excess and 100 ppm of H_2S, the overall selectivity reaches 47% at half conversion (54% if one includes cracking products, as in numerous publications). In most conditions, the cracking selectivity is lower than 1%. However, the ring-opening selectivity remains relatively low, *ca.* 5%.

For tetralin hydroconversion, Santikunaporn et al. have obtained RO, RC, and cracking selectivities of 16%, 21%, and 7%,

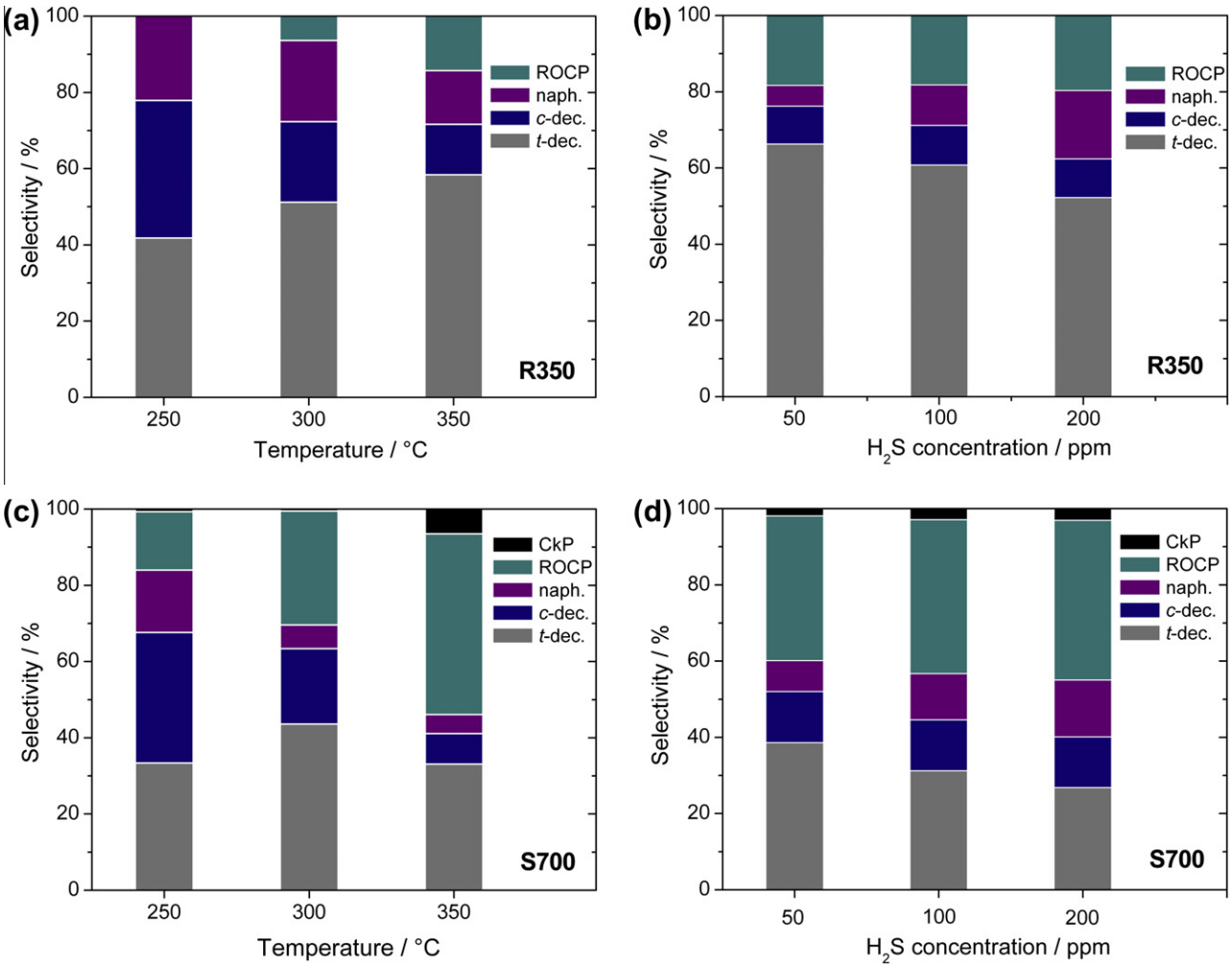

Fig. 12. Distribution of tetralin hydroconversion products for R350 and S700 Ir/ASA catalysts: (a and c) vs. temperature under 100 ppm H_2S at 50% tetralin conversion (except for S700 at 250 °C, 22% conversion); (b and d) vs. H_2S concentration at 350 °C and variable conversion.

respectively, for 1 wt.% Pt-HY at 325 °C, 93% conversion and in the absence of sulfur [14]. Arribas et al. have measured RO/RC/Ck selectivities of 16/50/10% and 20/50/20% for tetralin hydroconversion on 1 wt.% Pt-USY (275 °C) and 1 wt.% Pt-ITQ21 (300 °C), respectively, at total conversion and without sulfur [12,13]. By promoting a 0.5 wt.% Pt/USY catalyst with 1.2 wt.% potassium, Ma et al. have reduced the fraction of light products down to 5%, and measured RO/RC selectivities of 21/7% at 250 °C, again at total tetralin conversion and without sulfur [15]. Liu et al. claim RO/RC selectivities of 29/7% for Pt-HDAY at 280 °C and 87% conversion in the presence of thiophene, but with 15% of cracking products and important deactivation [16]. It must be noted that on these acid catalysts, more than 100 products of tetralin hydroconversion are formed [13,14].

However, all of these studies used conventional GC–MS for products identification, though in some cases complementary methods like analysis of GC retention times, boiling points or MS cracking patterns, comparison with GC standards, and/or kinetic checks were employed [9,10,14]. As we show in the present article, only bidimensional GC allows one to separate all products and, in particular, unambiguously discriminate ROPs from isomerization products in such complex mixtures. In addition, as already mentioned, saturated RCPs can easily be mistaken for olefinic ROPs when using standard MS databases [43,45].

An important conclusion of the above literature survey, confirmed by the present work, is that ring opening is in general combined with a high degree of isomerization (ring contraction). Although the satRCPs do not have CNs higher than those of saturated aromatics, under practical conditions they can be important intermediates to high-CN products, such as normal paraffins and some *iso*-paraffins [14].

In the work of Jiménez-López and coworkers, ROPs and RCPs have not been distinguished from each other. These authors have studied tetralin hydroconversion on various metals (Co, Ir, Pt, Pd, Rh, Ru Os, and some combinations) supported on Zr-doped mesoporous silica [18–20]. They have obtained, among more than 70 compounds, up to 50–60% of C_7–C_{10} cracking and isomerization products (which were not distinguished) on Ru and/or Os, accompanied with significant levels of volatile compounds (C_1–C_6) [19]. These catalysts deactivated gradually in the presence of dibenzothiophene. Recently, mesoporous aluminosilicate-supported PdRh catalysts have been assessed under similar conditions [21]. About 60% of "high molecular weight" products (the fraction of C_{10} RO products is not mentioned) were obtained at 350 °C for high tetralin conversion level. Catalytic tests in industrial conditions, aiming at treating a hydrogenated industrial light cycle oil containing less than 50 wt. ppm of sulfur, have shown that one of these PdRh catalysts was more efficient than a reference catalyst and led to a 7-point

cetane improvement at 280–300 °C [21]. A similar improvement has been achieved by Nylén et al. using $Ir_{95}Pt_5/CeO_2$ as a catalyst [28].

4.2. Interpretation of the metal particle size effect – mechanistic trends

Particle size effect is an old topic of heterogeneous catalysis by metals [6,46,47]. In our case, it would be tempting to relate the observed selectivity changes to the structure of Ir nanoparticles, *i.e.*, to a morphologic effect associated to the coordination of surface atoms: the smaller the particles, the higher the proportion of low-coordination sites. Depending on the adsorption sites, for relatively large molecules like tetralin derivatives (tetralin largest dimension is *ca.* 7 Å), the Ir particle size and morphology may influence how the adsorbate is accommodated to the surface (ensemble size effect).

An abundant literature deals with metal particle size effects in hydrogenolysis, including ring opening of one-ring naphthenes. The turnover rate of cyclopentane hydrogenolysis increases with particle size in the cases of Pt and Rh, while it is size insensitive for Ir [6]. In the case of Pt, small particles catalyze the ring opening of methylcyclopentane to a statistical mixture of 2-methylpentane, 3-methylpentane, and *n*-hexane, whereas *n*-hexane formation (from breaking of C—C bonds at substituted positions) is suppressed on large particles [48,49]. Ir favors selective hydrogenolysis with little effect of particle size [50]. For dimethylcyclohexane opening on Ir, the nature of the support would affect the selectivity. Indeed, C—C bond breaking at substituted positions is faster for Al_2O_3 than for SiO_2 [51]. In contrast, for Ir/SiO_2, an increased dispersion of Ir, tuned by K deposition, would favor metallocycle adsorption mode over dicarbene adsorption mode, leading to the cleavage of substituted C—C bonds [27].

In the case of two-ring hydrocarbons, the situation is even more intricate due to the various surface complexes which can be formed on the metal before hydrogenolysis, and the importance of the (acidic) support to achieve ring opening. To our knowledge, nothing has been published on the influence of metal particle size on bicyclic hydrocarbon ring opening.

However, the references cited above relate to hydrogenolysis on metal-based catalysts, whereas our Ir/ASA is bifunctional. For such a system, the acid-metal site balance is an important parameter [52]. To determine whether the observed metal particle size effect is intrinsic or generated by a change in acid/metal site ratio (N_{acid}/N_{metal}), we have prepared a R350-type sample with lower metal loading (0.22 wt.% Ir vs. 1 wt.% in other samples), in order to increase this ratio while keeping the Ir particle size constant ($\langle d \rangle_{surf} = 1.4 \pm 0.2$ nm). Fig. 14 reports the ROC selectivity of Ir/ASA catalysts (including the low-loaded one) as a function of N_{acid}/N_{metal}, which is calculated as follows:

$$\frac{N_{acid}}{N_{metal}} = \frac{M_{ASA},\ n_{acid},\ m_{Ir}}{M_{cat},\ L_{metal},\ D_{metal}}$$

M_{ASA}, n_{acid}, m_{Ir}, M_{cat}, L_{metal}, and D_{metal} denote ASA mass, Brönsted acid site (BAS) density, Ir molar mass, catalyst mass, metal loading, and metal dispersion, respectively. The BAS density on ASA (SIRAL-40) was estimated to 20 μmol g^{-1}.

Fig. 14 clearly evidences that R350(0.2%Ir) behaves like S500(1%), which has a similar N_{acid}/N_{metal} value but a different particle size, and not like R350(1%Ir), which has a similar particle size but a different N_{acid}/N_{metal} value. In other words, the selectivity to ROCPs increases continuously with the acid/metal site ratio, which appears as a relevant parameter for ROC selectivity.[6]

[6] Although the n_{acid} value is approximate, Fig. 14 shows that the high selectivity range explored here is associated to somewhat similar amounts of acid and metal sites, while the exposed metal surface represents less than 0.2% of the total catalyst surface.

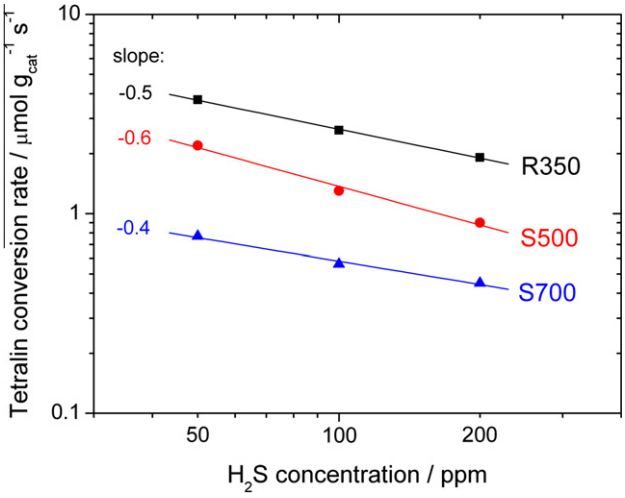

Fig. 13. Tetralin conversion rate vs. H_2S concentration for hydroconversion at 350 °C over three types of Ir/ASA samples. The pseudo-orders toward H_2S are indicated on the left-hand side.

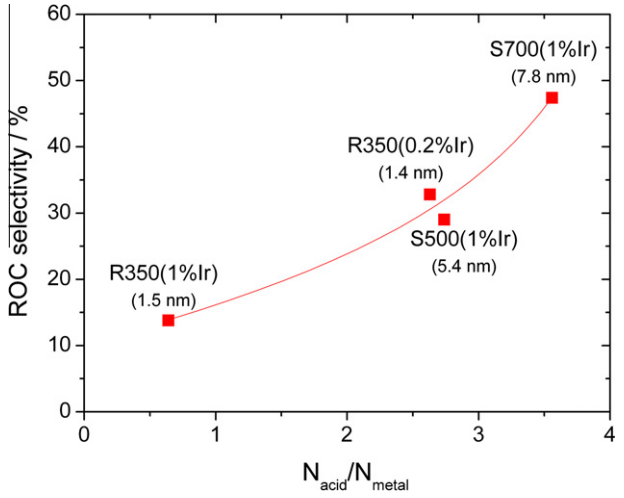

Fig. 14. Selectivity to ROCPs as a function of the acid/metal site ratio (see text). The metal loading and mean Ir particle size of the samples are indicated. Tetralin hydroconversion conditions: 350 °C, 100 ppm H_2S, 50% conversion, 50 mg of catalyst.

Several observations can now be understood in the light of this interpretation. Our thiotolerance data (Fig. 13) show that increasing Ir particle size does not affect H_2S orders. However, the simultaneous increase of the acid/metal site enhances the support's contribution to the reaction. This may in turn compensate the greater sulfur vulnerability of electron deficient (see XPS Table 2) large particles, since sulfur essentially inhibits metal-catalyzed hydrogenation. Such a compensation would explain the particle size-independent H_2S orders.

In another article [30], we show that the ROC selectivity of Ir/ASA scales with the Brönsted acidity of the catalyst (modified by changing ASA composition) and that no ROCPs are formed on Ir/SiO_2 or Ir/Al_2O_3, suggesting that ring opening and contraction are essentially Brönsted catalyzed. This is consistent with the fact that our products are, to a large extent, similar in nature to those formed on more acidic catalysts (Section 3.2.1). It follows

(Fig. 14) that an increase of the acid/metal site ratio (by changing the metal dispersion or loading) leads to an increase of the selectivity to ROCPs (and cracking products). In particular, the trends observed for *n*-butyl-benzene (major ROP) and branched/multi-substituted ROPs (Fig. 11) suggest that the former results from β-scission of a carbenium ion and that the latter are secondary Brönsted-catalyzed isomerization products. Conversely, the low variation of the selectivity to nBCH and nPCP indicates that these (minor) products may be formed by hydrogenolysis of bicyclic intermediates.

Our future work, through complementary kinetic experiments combined to GC×GC–MS analysis, will aim at further rationalizing the observed catalytic trends and proposing a mechanistic reaction scheme for tetralin hydroconversion on Ir/ASA.

5. Summary and conclusion

We have studied tetralin hydroconversion over Ir nanoparticles supported on amorphous silica–alumina (ASA) in a high-pressure flow micro-reactor (4 MPa H_2), in the presence of H_2S (up to 200 ppm). Our main results are summarized below:

- Sintering treatments of highly dispersed Ir nanoparticles (mean size 1.5 nm) at 500 °C and 700 °C in the presence of 2% H_2O lead to nanoparticles of 5.4 nm and 7.8 nm in size, respectively. HRTEM shows mainly truncated-octahedral particles. XPS shows that the nanoparticles are constituted of partially oxidized ($Ir^{\delta+}$) entities at the Ir–ASA interface and Ir^0 sites elsewhere.
- Tetralin is hydroconverted to naphthalene, decalins, C_{10} ring-contraction products (RCPs), and C_{10} ring-opening products (ROPs). RCPs are polycyclic molecules with at least one five-membered naphthenic ring, and ROPs are monocyclic molecules. Comprehensive two-dimensional GC–MS has allowed us, for the first time, to directly separate ROPs from RCPs (and saturated from aromatic products in each class) and determine the selectivity of each individual product. Among ROPs, *n*-butyl-benzene is the most abundant compound.
- Ir/ASA catalysts are sulfur tolerant, since they deactivate only partially upon H_2S introduction in the reactant feed, and recover their activity after H_2S removal. As, in addition, the level of cracking is low (<7% of products with less than 10 carbon atoms, in all cases), the catalysts show stable activity over days. While the hydrogenation/dehydrogenation product ratio decreases as the H_2S concentration increases, the sulfur content in the 50–200 ppm range has no effect on the selectivity to ring-opening/contraction products.
- The ring-opening/contraction selectivity increases with temperature and Ir particle size. For 7.8 nm particles, it reaches 47% (5% ROPs) at 350 °C (50% conversion, 100 ppm H_2S). A decrease of the metal loading of a non-sintered Ir/ASA is equivalent, in terms of ring-opening/contraction selectivity, to an increase of the Ir particle size, provided that the acid/metal site ratio is kept constant. The apparent metal particle size effect thus originates from a change in acid-metal site balance.

In conclusion, Ir/ASA is a stable thiotolerant bifunctional catalyst for tetralin hydroconversion. Tuning the Ir particle size has allowed us to dramatically increase the selectivity toward ring-opening/contraction products. For diesel upgrading purposes, a better understanding of the bifunctional reaction mechanism is now needed to orient the reaction toward high-cetane-number ring-opening products through further catalyst modifications, such as metal alloying.

Acknowledgments

S. Nassreddine thanks the French government for his PhD grant. We thank Sasol Germany GmbH for the supply of the SIRAL-40 sample. P. Delichère, L. Burel, G. Toussaint, C. Lorentz, and N. Cristin are greatly acknowledged for their support in XPS, TEM, GC×GC–MS, NMR, and ICP-OES analyses, respectively. S. Casu and J.L. Zotin (Petrobras) are acknowledged for early experiments and support, respectively.

References

[1] B.H. Cooper, B.B.L. Donnis, Appl. Catal. A 137 (1996) 203.
[2] G.B. McVicker, M.S. Touvelle, C.W. Hudson, D.E.W. Vaughan, M. Daage, S. Hantzer, D.P. Klein, E.S. Ellis, B.R. Cook, O.C. Feeley, J.E. Baumgartner, World Patent WO9709288, 1997.
[3] G.B. McVicker, M. Daage, M.S. Touvelle, C.W. Hudson, D.P. Klein, W.C. Baird Jr., B.R. Cook, J.G. Chen, S. Hantzer, D.E.W. Vaughan, E.S. Ellis, O.C. Feeley, J. Catal. 210 (2002) 137.
[4] R.C. Santana, P.T. Do, M. Santikunaporn, W.E. Alvarez, J.D. Taylor, E.L. Sughrue, D.E. Resasco, Fuel 85 (2006) 643.
[5] H. Du, C. Fairbridge, H. Yang, Z. Ring, Appl. Catal. A 294 (2005) 1.
[6] F.G. Gault, Adv. Catal. 30 (1981) 1.
[7] J.H. Sinfelt, Catal. Rev. 3 (1969) 175.
[8] Z. Paal, Adv. Catal. 29 (1980) 273.
[9] D. Kubicka, N. Kumar, P. Mäki-Arvela, M. Tiitta, V. Niemi, T. Salmi, D.Y. Murzin, J. Catal. 222 (2004) 65.
[10] D. Kubicka, N. Kumar, P. Mäki-Arvela, M. Tiitta, V. Niemi, H. Karhu, T. Salmi, D.Y. Murzin, J. Catal. 227 (2004) 313.
[11] A. Corma, V. González-Alfaro, A.V. Orchillés, J. Catal. 200 (2001) 34.
[12] M.A. Arribas, P. Conceptión, A. Martínez, Appl. Catal. A 267 (2004) 111.
[13] M.A. Arribas, A. Corma, M.J. Díaz-Cabañas, A. Martínez, Appl. Catal. A 273 (2004) 277.
[14] M. Santikunaporn, J.E. Herrera, S. Jongpatiwut, D.E. Resasco, W.E. Alvarez, E.L. Sughrue, J. Catal. 228 (2004) 100.
[15] H. Ma, X. Yang, G. Wen, G. Tian, L. Wang, Y. Xu, B. Wang, Z. Tian, L. Lin, Catal. Lett. 116 (2007) 149.
[16] H. Liu, X. Meng, D. Zhao, Y. Li, Chem. Eng. J. 140 (2008) 424.
[17] S. Albertazzi, R. Ganzerla, C. Gobbi, M. Lenarda, M. Mandreoli, E. Salatelli, P. Savini, L. Storaro, A. Vaccari, J. Mol. Catal. A 200 (2003) 261.
[18] E. Rodríguez-Castellón, J. Mérida-Robles, L. Díaz, P. Maireles-Torres, D.J. Jones, J. Rozière, A. Jiménez-López, Appl. Catal. A 260 (2004) 9.
[19] D. Eliche-Quesada, J.M. Mérida-Robles, E. Rodríguez-Castellón, A. Jiménez-López, Appl. Catal. A 279 (2005) 209.
[20] A. Infantes-Molina, J. Mérida-Robles, E. Rodríguez-Castellón, J.L.G. Fierro, A. Jiménez-López, Appl. Catal. B 73 (2007) 180.
[21] M. Taillades-Jacquin, D.J. Jones, J. Rozière, R. Moreno-Tost, A. Jiménez-López, S. Albertazzi, A. Vaccari, L. Storaro, M. Lenarda, J.M. Trejo-Menayo, Appl. Catal. A 340 (2008) 257.
[22] K. Chandra Mouli, V. Sundaramurthy, A.K. Dalai, Z. Ring, Appl. Catal. A 321 (2007) 17.
[23] V. Calemma, M. Ferrari, M.F. Gagliardi, F. Baldiraghi, World Patent WO09106324, 2009.
[24] J. Barbier, E. Lamy-Pitara, P. Marécot, J.P. Boitiaux, J. Cosyns, F. Verna, Adv. Catal. 37 (1990) 279.
[25] S. Lecarpentier, J. van Gestel, K. Thomas, J.P. Gilson, M. Houalla, J. Catal. 254 (2008) 49.
[26] Z. Wang, A.E. Nelson, Catal. Lett. 123 (2008) 226.
[27] S.L. González-Cortés, S. Dorkjampa, P.T. Do, Z. Li, P.T. Do, Z. Li, J.M. Ramallo-López, F.G. Requejo, Chem. Eng. J. 139 (2008) 147.
[28] U. Nylén, L. Sassu, S. Melis, S. Järås, M. Boutonnet, Appl. Catal. A 299 (2006) 1.
[29] S. Nassreddine, G. Bergeret, B. Jouguet, C. Geantet, L. Piccolo, Phys. Chem. Chem. Phys. 12 (2010) 7812.
[30] S. Nassreddine, S. Casu, J.L. Zotin, C. Geantet, L. Piccolo, submitted for publication.
[31] S. Balcon, S. Mary, C. Kappenstein, E. Gengembre, Appl. Catal. A 196 (2000) 179.
[32] M. Vrinat, L. de Mourgues, React. Kinet. Catal. Lett. 14 (1980) 389.
[33] F. Labruyère, M. Lacroix, D. Schweich, M. Breysse, J. Catal. 167 (1997) 464.
[34] V.N. Bui, G. Toussaint, D. Laurenti, C. Mirodatos, C. Geantet, Catal. Today 143 (2009) 172.
[35] S.E. Reichenbach, M. Ni, V. Kottapalli, A. Visvanathan, Chemom. Intell. Lab. Syst. 71 (2004) 107.
[36] W. Daniell, U. Schubert, R. Glöckler, A. Meyer, K. Noweck, H. Knözinger, Appl. Catal. A 196 (2000) 247.
[37] L.C. Gontard, L.Y. Chang, C.J.D. Hetherington, A.I. Kirkland, D. Ozkaya, R.E. Dunin-Borkowski, Angew. Chem. Int. Ed. 46 (2007) 3683.
[38] M. Peuckert, Surf. Sci. 144 (1984) 451.
[39] S. Thanawala, D.G. Georgiev, R.J. Baird, G. Auner, Thin Solid Films 515 (2007) 7059.
[40] NIST XPS Database. <http://srdata.nist.gov/xps/>.
[41] P. Reyes, M.C. Aguirre, G. Pecchi, J.L.G. Fierro, J. Mol. Catal. A 164 (2000) 245.

[42] J.C. Bertolini, P. Delichère, B.C. Khanra, J. Massardier, C. Noupa, B. Tardy, Catal. Lett. 6 (1990) 215.
[43] C. Flego, N. Gigantiello, W.O. Parker Jr., V. Calemma, J. Chromatogr. A 1216 (2009) 2891.
[44] L.S. Golovkina, G.V. Rusinova, A.A. Petrov, Russ. Chem. Rev. 53 (1984) 870 (and references therein).
[45] L. Piccolo, S. Nassreddine, G. Toussaint, C. Geantet, J. Chromatogr. A 1217 (2010) 5872.
[46] M. Che, C.O. Bennett, Adv. Catal. 36 (1989) 55.
[47] B. Coq, F. Figueras, Coord. Chem. Rev. 178–180 (1998) 1753.
[48] R. Kramer, H. Zuegg, J. Catal. 80 (1983) 446.
[49] R. Kramer, H. Zuegg, J. Catal. 85 (1984) 530.
[50] J.G. van Senden, J. Catal. 87 (1984) 468.
[51] P.T. Do, W.E. Alvarez, D.E. Resasco, J. Catal. 238 (2006) 477.
[52] C. Marcilly, Acido-Basic Catalysis: Applications to Refining and Petrochemistry (Ed.), Technip, Paris, 2005.